Stiffness, Strength, and Toughness of Electrospun Nanofibers: Effect of Flow-Induced Molecular Orientation

Israel Greenfeld,* XiaoMeng Sui, and H. Daniel Wagner

Department of Materials and Interfaces, Weizmann Institute of Science, Rehovot 76100, Israel

Ⓢ *Supporting Information*

ABSTRACT: The simultaneous sharp rise in stiffness, strength, and toughness of electrospun nanofibers at small diameters is explained here as the result of the molecular orientation induced by the strong stretching of the electrospinning extensional flow. Differing from the common view that this phenomenon is related to the nanofibers size scale, we show by theoretical analysis that it is likely the result of an abrupt transition in polymer chain extension that occurs at high flow strain rates. Consequently, the molecular orientation and mechanical properties experience a matching transition, followed by a linear rise with the strain rate. The model

compares well with published experimental data, supporting the assertion that the observed phenomena can be explained as the consequence of electrospinning conditions instead of size dependence. We show how the mechanical properties can be tuned by controlling the process as well as set the goal for future improvement in these properties.
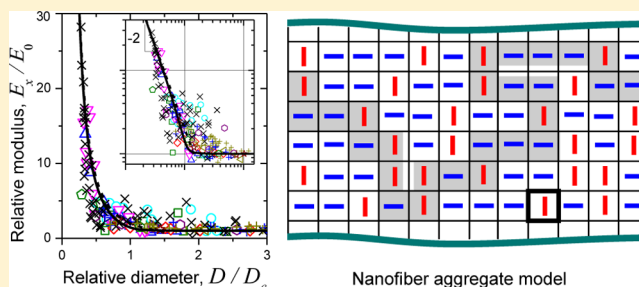
INTRODUCTION

Electrospun polymeric nanofibers exhibit so-called size-dependent properties, such as a significant increase in their stiffness (tensile modulus), strength, and toughness below a certain critical diameter.[1−12] It was shown that the critical diameter varies across a wide range of values, from ∼100 nm to ∼10 μm,[1−10,12] and depends on the polymer molar mass.[2] The relationship between size and modulus was observed also in materials other than polymers,[13−15] suggesting a universal phenomenon; however, the mechanism is not necessarily the same.

A common view is that this change in mechanical properties is related to size scale through boundary and confinement effects. Boundary effects include surface tension[13−17] (found to be negligible in nanofibers)[7] as well as molecular orientation induced by the boundary.[2] A core−shell morphology was also suggested, where the nanofiber shell is dense and stiff as a result of rapid solvent evaporation, increasingly dominating the properties as its volume fraction increases with decreasing diameter.[9,12] Other heterogeneous structures showed an opposite trend with a dense and stiff core having high molecular alignment.[18−20] The degree of crystallinity in semicrystalline polymers was also shown to depend on diameter, where in some cases it increased at small diameters[1] while in others it decreased.[10] Confinement effects assume ordered supramolecular structures, whose size is of the same scale as the nanofiber diameter, and therefore their rotation under stress is hindered by the boundary.[1,21,22] However, the existence of such supramolecular structure lacks direct experimental support[11] and does not explain the modulus rise when the critical diameter is several micrometers.[2,5,11,12]

The mechanisms described above imply a direct influence of the nanoscale diameter on the rise of the mechanical properties, either by locally enhancing molecular orientation and degree of crystallinity or by confining ordered supramolecular substructures. However, these mechanisms do not account for the effects of the extremely strong extensional flow on the polymer network structure prior to solidification, particularly the partial retraction of polymer chains from the network and the segmental orientation of these chains.[19,23] Molecular orientation was shown to increase with decreasing fiber diameter and to positively correlate with the elastic modulus,[6,12] as observed and modeled by Pai et al. using an aggregate model.[6] The orientation was shown to positively correlate also with the degree of disentanglement.[12] In addition to modeling these dependencies, there is a need for a theoretical model that relates electrospinning conditions to molecular orientation and shows its consequence on the mechanical properties of nanofibers.

Hence, in the current study we seek to explain the stiffness, strength, and toughness rise by means of the molecular orientation induced by the extensional flow of electrospinning. We show by theoretical modeling that chain extension undergoes an abrupt transition at high strain rates and that this transition is the likely cause for the sharp rise in molecular orientation and modulus. In that context, we say that the term size dependence is somewhat misleading, as it implies a direct effect of the diameter on the modulus. Rather, the diameter and

modulus are shown to be separately dependent on the flow's strain rate and are therefore related by association and not by cause. The same approach is extended to strength and toughness. The mechanical properties are modeled using an aggregate representation of the nanofiber, and the theoretical results are compared with experimental evidence imported from published studies. The reinforcement of nanofibers with nanofillers such as carbon nanotubes (CNTs) is also briefly discussed.

■ CHAIN ELONGATION DURING EXTENSIONAL FLOW

The strong extensional flow of a polymer solution, such as the flow of an electrospinning jet (Figure 1a), requires that the
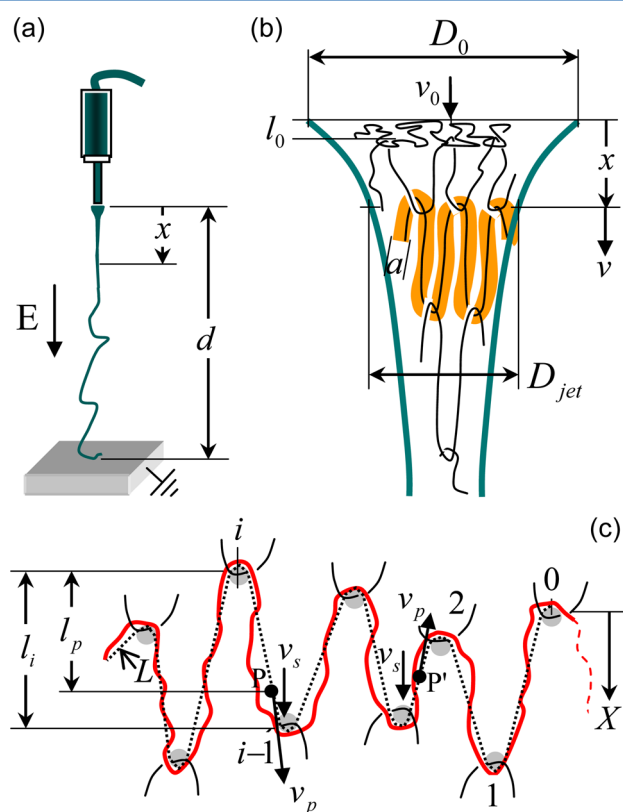
Figure 1. Illustration of chain dynamics in extensional flow and definition of parameters. (a) Electrospinning under electrostatic field intensity E (not to be confused with the modulus E). (b) Polymer network extension and partial retraction, showing the jet boundary (turquoise) and a typical confining tube a (orange). (c) The left half of a typical chain (red) and its primitive path L (dotted line). The gray circles represent entanglement nodes, numbered sequentially 0, 1, 2, ..., i starting from the chain center 0. The thick arrows indicate the polymer and solvent velocity vectors with respect to the chain center, v_p and v_s, respectively, at points P and P′.

solution be semidilute entangled, in order to ensure the strength and continuity of the jet and the eventual creation of nanofibers.[23] The polymer structure in such solutions is a network of entangled polymer chains immersed in solvent, which, when subjected to an extensional flow, is stretched by the hydrodynamic forces.[24] In turn, chains gradually retract (untangle) from the polymer network by a dynamic process involving stretching, reptation, and relaxation.[25−29] The entanglement loss rate is faster when the flow's strain rate is

high, the chains are short, and the polymer concentration is low.

The degree of chain extension, and consequently its molecular orientation, are the result of the competing dynamics of stretching and partial retraction. Entanglements, topological constraints that prevent intercrossing of chains, effectively divide each polymer chain into strands, which are elastically stretched under the applied extensional forces. At equilibrium, when the solution is at rest, chains can reptate within a confining tube (Figure 1b), defined by the constraining potential of nearby chains, allowing monomers to fluctuate within its diameter.[30−32] Under strain, chains can relieve some of the high elastic tension by sliding along the tube and partial retraction, thereby achieving a new state of equilibrium.[25−29]

The rheology of entangled polymer solutions subjected to extensional flow has been widely investigated,[33−37] using constitutive models based on the confining tube and chain reptation concepts.[30,31] Here, we present a mechanical model of a single entangled chain immersed in the extensional flow of an electrospinning jet and use this model to derive the evolution of chain extension and molecular orientation and the ensuing nanofiber diameter and mechanical properties.

Consider the typical entangled polymer chain, whose left half is shown in Figure 1c, subjected to the elongational flow of a vertically aligned electrospinning jet. The primitive path length of the chain half (the dotted zigzag line) is L. The chain consists of strands extending between entanglement nodes (represented by the gray circles). The end-to-end length of a strand i is approximately l_i, the vertical distance between nodes i and $i − 1$. Given the jet vertical velocity v and velocity gradient ∇v (that is, strain rate), both functions of the vertical distance x from the jet start, a node i moves at velocity $v_i = X_i \nabla v$ with respect to the chain center, where X is a local vertical axis attached to the chain center (point 0 in Figure 1c). Nodes located above the chain center move upward with respect to it ($X_i < 0$), while those below the center move downward ($X_i > 0$).

In this we assume that the entanglement nodes are moving at the same velocity as the jet, with negligible local velocity lag or lead, in other words an affine deformation of the polymer network.[23,24] We also assume that ∇v is practically constant within the small size scale of a single chain. As a result, lower nodes are moving downward faster than higher ones, continually increasing their vertical separation, dragging the two chain halves extending from the chain center and causing the chain to simultaneously elongate and slide within its confining tube.

By analogy to a rope in a system of pulleys, the end-to-end elongation of each strand contributes a velocity magnitude $l_i \nabla v$ to the dragging velocity of the chain along its primitive path. The cumulative contribution of preceding strands to the velocity of a strand l_i is of magnitude $\sum_{j=1}^{i-1} l_j \nabla v = L_{i-1} \nabla v$, where L_{i-1} is the distance from node 0 to node $i − 1$ along the primitive path. Node $i − 1$ drags the strand l_i downward at velocity $X_{i-1} \nabla v$, and therefore the overall downward velocity of the strand is $v_p \cong (X_{i-1} + L_{i-1}) \nabla v$ with respect to the chain center. At a point P, located a distance l_p below node i (Figure 1c), the solvent flows downward at velocity $v_s \cong X_p \nabla v = (X_i + l_p) \nabla v$ with respect to the chain center. Thus, the chain downward velocity with respect to the solvent is given by

$$v_p - v_s \cong [L_{i-1} + (X_{i-1} - X_i) - l_p]\nabla v$$
$$\cong (L_i - l_p)\nabla v \cong L_p \nabla v, \quad 0 \le L_p \le L \tag{1}$$

where L_p is the distance from node 0 to point P along the primitive path. Similarly, at a point P' (Figure 1c), $v_p \cong (X_{i-1} - L_{i-1})\nabla v$ and $v_s \cong (X_i - l_p)\nabla v$, yielding an upward velocity of $v_p - v_s \cong -L_p\nabla v$. Hence, a chain section at an arbitrary point P experiences a solvent velocity of magnitude $L_p\nabla v$ in the pathwise direction toward its free end and a corresponding proportional hydrodynamic force. More generally, when the chain is rotated with respect to x, the chain pathwise velocity should be adjusted by an orientation term, for example, $L_p\nabla v \cos\theta$ (or just $L_p\nabla v$ if the orientation term is implicitly included in ∇v), where θ is the flow-dependent rotation angle.

The solvent velocity with respect to chain sections grows linearly from 0 at the chain center up to a maximum of $L\nabla v$ at its ends ($L_p = L$). Consequently, the hydrodynamic force acting on the chain produces a shear stress that is lower close to its center and higher toward its ends. The integration of the shear stress from the free ends toward the center generates tension in the chain, which builds up from zero at the free ends up to a maximum at the center, evidenced by a preferred midpoint chain scission in extensional flow experiments.[38−40] As a result, the degree of chain extension and segmental orientation is not uniform along the chain but rather decreases with the distance from the center outward. However, because we are interested in average scaling properties of the chain (average orientation, average elastic modulus, etc.), we are justified in using an average velocity $L\nabla v/2$.

The average hydrodynamic force acting on the chain half, $\zeta L\nabla v/4$ where ζ is the hydrodynamic friction coefficient of the full chain, gives rise to an average elastic tension $F(L)$ in the chain. The elasticity of a polymer chain is entropic; in other words, its entropy decreases and hence its stiffness increases for less probable chain conformations, and therefore at very large elongations $F(L)$ rises sharply and deviates strongly from linear behavior. The chain dynamics can be described by the following differential equation:

$$m\frac{d^2L}{dt^2} - \zeta\left(L\nabla v - \frac{dL}{dt}\right) + 4[F(L) - F(L_0)] \approx 0 \tag{2}$$

where the $\approx$ symbol denotes a scaling relationship, m is the chain mass, and $F(L_0)$ is the effective elastic force when the network is at rest, corresponding to a primitive path length L_0. The time derivatives of L denote the average pathwise velocity and acceleration of the chain half, resulting from its extension (positive derivatives of L). The hydrodynamic friction coefficient scales as (see Appendix)

$$\zeta \approx \eta_s b N \phi^{(1-\nu)/(3\nu-1)} \tag{3}$$

where η_s is the solvent viscosity, b is the monomer length, N is the number of monomers in the chain (that is, the degree of polymerization), ϕ is the polymer volume fraction (that is, volume concentration), and ν is Flory's exponent (1/2 for a θ-solvent and approximately 0.588 for a good solvent[32]). The term monomer is used here in the sense of a Kuhn monomer, that is, a chain section that can be considered rigid, typically containing several chemical monomers.

Because our main interest is in the average segmental orientation of the chain, we substitute the chain primitive path

semilength L by the average relative extension of the chain ε, defined as

$$\varepsilon \equiv \frac{L}{L_{max}} = \frac{2L}{bN} \tag{4}$$

Substituting ε and ζ into eq 2 and rearranging:

$$\tau_m\frac{d^2\varepsilon}{dt^2} - \left(\varepsilon\nabla v - \frac{d\varepsilon}{dt}\right) + \frac{1}{\tau}[f(\varepsilon) - f(\varepsilon_0)] \approx 0 \tag{5}$$

where $\tau_m = m/\zeta \approx m_0/(\eta_s b\phi^{(1-\nu)/(3\nu-1)})$ is a characteristic time due to the chain mass (m_0 is the mass of a single Kuhn monomer) and

$$\tau \approx \tau_0 N^2\phi^{(1-\nu)/(3\nu-1)} \tag{6}$$

is the relaxation time of an extended chain, where $\tau_0 \approx \eta_s b^3/(k_B T)$ is the relaxation time of a single monomer,[32] k_B is Boltzmann constant, and T is the temperature. The component $\tau_R \approx \tau_0 N^2$ is the Rouse chain relaxation time. The exponent of ϕ is 0.54 for a good solvent and 1 for a θ-solvent. Constants of order unity were omitted. $f = Fb/(k_B T)$ is the normalized force, and $\varepsilon_0 = L_0/L_{max}$ is the primitive path initial extension of a chain in a network at rest (see Appendix).

Because $\tau_m \ll \tau$ ($\tau_m \sim 10^{-12}$ s for common polymers and solutions, and $\tau \sim 10^{-4}-10^{-2}$ s for typical electrospinning solutions), the effect of chain acceleration can be neglected, reducing eq 5 to

$$\frac{d\varepsilon}{dt} \approx \varepsilon\nabla v - \frac{1}{\tau}[f(\varepsilon) - f(\varepsilon_0)] \tag{7}$$

This stretch equation is equivalent to the uniaxial extensional flow model of Bhattacharjee et al.,[36] as can be seen by substituting $f(\varepsilon_0) \cong 3\varepsilon_0$ and switching to the stretch ratio $\lambda = L/L_0$ by substituting $\varepsilon = \varepsilon_0\lambda$. The flow-dependent tube orientation term,[36] implicitly included in ∇v, reduces the resultant stretching at low strain rates (nearly random orientation), while tending to 1 at high strain rates (nearly uniform orientation). Therefore, when the orientation term is not explicitly used, eq 7 can be regarded as an upper bound for chain extension, with a close match at high strain rates.

Switching from the time domain t to the jet velocity domain v (by substituting $d\varepsilon/dt = (d\varepsilon/dv)v\nabla v$):

$$\frac{d\varepsilon}{dv} \approx \frac{\varepsilon}{v}\left[1 - \frac{f(\varepsilon) - f(\varepsilon_0)}{\nabla v\tau\varepsilon}\right] \tag{8}$$

The initial condition at $t = 0$ (or $v = v_0$, the initial velocity) is $\varepsilon = \varepsilon_0$, given by (see Appendix)

$$\varepsilon_0 \approx \frac{L_0}{L_{max}} \approx \begin{cases} \phi^{(1-\nu)/(3\nu-1)} & \text{good solvent} \\ \phi^{2/3} & \theta\text{-solvent} \end{cases} \tag{9}$$

Typical values are $\varepsilon_0 \cong 0.01-0.3$.

The velocity profile of a jet in an extensional flow, specifically electrically driven fluid jets, can be described (sufficiently far from the jet exit) by a power law of the form $v/v_0 \cong (sx/v_0)^{2\beta}$, where β ranges from 1/4 to 1 and s is the gradient constant.[41−46] This allows us to express the velocity gradient in eq 8 in terms of the velocity, $\nabla v \approx s(v/v_0)^\gamma$, where $\gamma = (2\beta - 1)/(2\beta)$ ranges from −1 (decreasing gradient), through 0 (constant gradient, s), to 1/2 (increasing gradient). The evolution of ε and $f(\varepsilon)$ as functions of the jet relative velocity v/v_0 is depicted in Figure 2, for three types of velocity gradient:
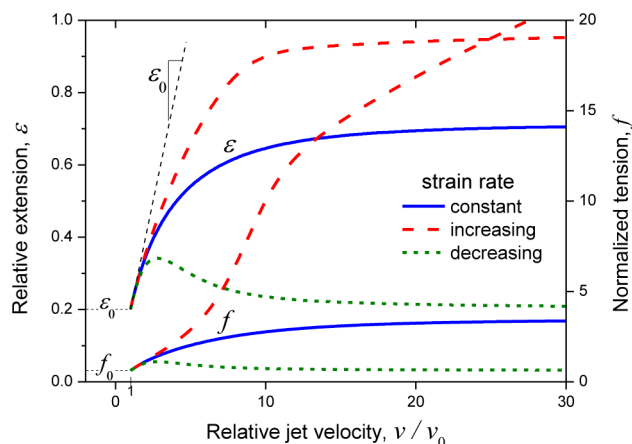
Figure 2. Chain extension ε and tension force $f(\varepsilon)$ based on eq 8, as functions of the jet relative velocity v/v_0, for decreasing, constant and increasing velocity gradients (strain rates), $s(v/v_0)^{-1}$, s, and $s(v/v_0)^{0.5}$, respectively. $\varepsilon_0 = 0.2$, $s\tau = 4$, $f(\varepsilon)$ is defined by an inverse Langevin function (see text), and $f_0 = f(\varepsilon_0)$.

increasing, constant, and decreasing. For a constant gradient, ε reaches a stable steady-state value, whereas for an increasing gradient it is asymptotic to $\varepsilon = 1$, and for an decreasing gradient it is asymptotic to $\varepsilon = \varepsilon_0$. Because of the very rapid solvent evaporation during electrospinning,[47−51] increasing and decreasing gradients may eventually saturate into a constant gradient, as indeed observed in common electrospinning processes[46,52,53] (see Supporting Information section S6).

The onset of bending (whipping) instability causes the jet to form a sequence of smoothly curved loops, generating a considerable jet elongation that can theoretically mount up to 10^5 s^{-1}.[54,55] However, measurements show that this value is moderated by evaporation and partial solidification to an average strain rate of 10^3 s^{-1}. A possible strain rate change during the transition from the jet's straight regime to the whipping regime would indeed have an effect on the relative chain extension ε. However, this does not affect the validity of the chain dynamics analysis described above but only changes the value of the strain rate in the model. See further details in Supporting Information section S6.

Hence, we focus on the case of a constant velocity gradient, $\nabla v = s \sim 10^3-10^5$ s^{-1}, in which eq 8 has a single parameter $s\tau$, and can be solved by separation of variables for a given function of the elastic force $f(\varepsilon)$. The dimensionless parameter $s\tau$ is of order 10^0-10^2 for common electrospinning conditions. $s\tau$ determines the balance between the hydrodynamic stretching force and the opposing elastic (entropic) contraction force. When $s\tau$ is high, the hydrodynamic force is dominant and the extension is strong, whereas when $s\tau$ is low the elastic force is dominant and the extension is weak.

◼ STEADY STATE CHAIN EXTENSION

The transient response of ε is exponential, with a characteristic time constant inversely proportional to the velocity gradient (eq 7 with $f(\varepsilon) \cong f(\varepsilon_0)$), of the order of $s^{-1} \sim 10^{-5}-10^{-3}$ s. This rise time is very fast, occurring within the first few millimeters of the jet, prior to a significant onset of solidification. During that stage, ε rises approximately linearly with v (eq 8 with $f(\varepsilon) \cong f(\varepsilon_0)$):

$$\frac{\varepsilon}{\varepsilon_0} \approx \frac{v}{v_0} \tag{10}$$

as expected from the affine deformation of the polymer network.[23,24]

Because a steady state extension is achieved early on, a time-dependent solution of eq 8 is not needed for our purpose. Instead, the steady state extension and tension can be derived by (eq 7 with $d\varepsilon/dt = 0$):

$$s\tau\varepsilon \cong f(\varepsilon) - f(\varepsilon_0) \tag{11}$$

for a known function of the elastic force $f(\varepsilon)$. Estimates can be obtained using the Langevin nonlinear force function,[32] $\varepsilon = \mathcal{L}(f) \equiv \coth(f) - 1/f$, in its inverse form $f = \mathcal{L}^{-1}(\varepsilon)$, for which we use the approximation[56] $f \cong \varepsilon(3 - \varepsilon^2)/(1 - \varepsilon^2)$. Alternative similar nonlinear force functions can be applied, for example, $f \cong 3\varepsilon(1 - \varepsilon_0)/(1 - \varepsilon)$ (adapted from Bhattacharjee et al.[36]). Numerical solution of ε and $f(\varepsilon)$ for three values of ε_0 is presented in Figure 3. Explicit solution of eq 11 may be
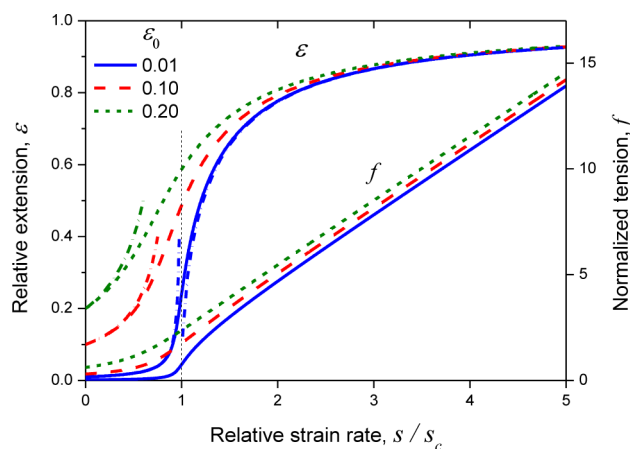
Figure 3. Steady state chain extension ε and tension force f as functions of the relative strain rate s/s_c, where $s_c = 3\tau^{-1}$ is the critical strain rate and τ is the chain relaxation time. Numerical solution of eq 11, for three initial extensions ε_0, including the approximations of eqs 12 and 13 (dash-dotted lines).

obtained by solving the resultant cubic equation, but this is too long and lacks insight. Alternatively, series expansion approximations can be obtained for small extensions by using $f(\varepsilon) \cong 3\varepsilon$ from the force function

$$\varepsilon \cong \frac{\varepsilon_0}{1 - s\tau/3} \cong \varepsilon_0\left(1 + \frac{s\tau}{3}\right), \quad s\tau < 3 \tag{12}$$

where the right term is for $s\tau \ll 3$. Similarly, for high extensions by using $f(\varepsilon) \gg f(\varepsilon_0)$ in eq 11, yielding

$$\varepsilon \cong \sqrt{\frac{s\tau - 3}{s\tau - 1}} \cong 1 - \frac{1}{s\tau}, \quad s\tau > 3 \tag{13}$$

where the right term is for $s\tau \gg 3$. These two approximations are presented in Figure 3 as well.

If the external tension is removed too early, for example when the jet reaches the collector in a liquid state, the extended strands will relax (recoil back to equilibrium conformation) within a characteristic time τ. However, because the strand extension ε stabilizes early in the process, and because in general the jet is largely solidified when it hits the collector, the extension magnitude is essentially retained in the solid nanofiber. Further relaxation of stretched chains is minimal for polymers with a high glass transition temperature T_g. Note that the recoiling characteristic time τ should not be confused

with reptation time, the time for an entangled chain to diffuse along its primitive contour length.

The stabilized chain extension ε derived from eqs 11 and 12 goes through an abrupt transition at $s\tau = 3$, seen in Figure 3. We define the critical strain rate as the strain rate at this transition point:

$$s_c = \frac{3}{\tau} \tag{14}$$

and further define the relative strain rate, $s/s_c = s\tau/3$. The relative strain rate depends on the electrospinning process parameters, as shown in eq 30. At the transition point $(s\tau = 3)$, the critical steady state extension can be approximated by series expansion of eq 11 at accuracy of $O(\varepsilon_0{}^2)$:

$$\varepsilon_c \cong \left(\frac{3\varepsilon_0}{2}\right)^{1/3} - \frac{\varepsilon_0}{2}, \quad s\tau = 3 \tag{15}$$

We observe that the chain demonstrates two distinct equilibrium states with respect to the strain rate s: when $s < s_c$, the strand is slightly stretched but remains in a conformation close to a Gaussian coil, whereas when $s > s_c$, the strand goes to an almost fully stretched state. A phase transition occurs at the critical gradient, $s = s_c$, with two widely separated extension states: the coil shape and the stretched shape. This phenomenon is similar to the known coil stretch transition observed in a free unentangled chain in an extensional flow field[30,57] and implies the existence of two distinct energy equilibrium states that correspond to the two extension states. Coil stretch transition was also observed in entangled polymer chains under an extensional flow, for example, by Odell et al.[58] and Bhattacharjee et al.[36] The discussion in the next section will show how this transition drives a consequent transition in the elastic modulus of electrospun nanofibers.

■ MOLECULAR ORIENTATION

Given the relative extension of a chain ε, its average segmental orientation O can be calculated, where a segment is a rigid section of a chain referred to as a Kuhn segment (or Kuhn monomer)[32] of size b. A flexible linear polymer chain with N segments can be described by N successive steps of length b on a 3D Cartesian lattice, where a step represents a single monomer.[30,32,59] Such a chain is illustrated in 2D in Figure 4 by the gray sequence of segments. The stepping direction is determined by the effective external potential U at the monomer position, arising from the initial state of the polymer network and the hydrodynamic force exerted on it. The probability that a step (that is a monomer) will be in a given direction is $e^{-\nabla Ub/(k_B T)}/Q$, where ∇U is the potential gradient in that direction, ∇Ub is the potential rise along the step, and Q is a partition function.[59,60]

Within the framework of a jet, we define the Cartesian system x, y, z, so that x is the downward longitudinal axis (Figures 1a and 4), and y and z are the outward radial axes. We denote the potential step in the longitudinal direction as $u_x = u = \nabla U_x b/(k_B T)$. In the radial directions, the potential gradient induced by the flow is negligible,[24,59] and therefore we denote $u_y = u_z = u_0$, where u_0 is the potential step for a polymer network at rest. The probability that a monomer will be oriented in the positive (+) or negative (−) directions of the longitudinal axis or one of the two radial axes is given by
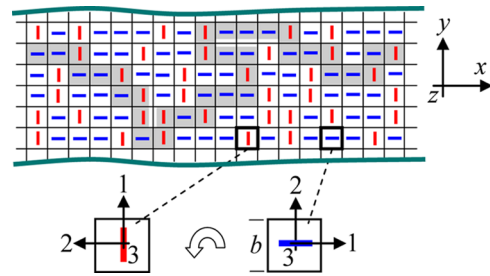
Figure 4. Illustration of a polymer chain (gray) consisting of a sequence of connected segments b on a Cartesian lattice, residing within the boundary (turquoise) of a jet or a nanofiber. The global axes system is denoted by x, y, z. In the solid state, the nanofiber is represented by an aggregate consisting of dispersed unit elements of size b, whose local axes system is denoted by 1, 2, 3, where (1) represents the high stiffness direction (chain backbone bonds) and (2, 3) the low stiffness directions (interchain bonds). An element can be oriented in the x direction (blue) or in a lateral (radial) y or z direction (red).

$$P_x^\pm = \frac{e^{\mp u}}{2(\cosh u + 2\cosh u_0)}$$

$$P_y^\pm = P_z^\pm = \frac{e^{\mp u_0}}{2(\cosh u + 2\cosh u_0)} \tag{16}$$

where Q was determined so that the sum of all probabilities equals 1.

The chain extension is the sum of the lengths of all monomers oriented in the positive longitudinal direction, minus the sum of all monomers oriented in the negative longitudinal direction, and hence the relative extension is given by

$$\varepsilon = \varepsilon_x = P_x^+ - P_x^- = \frac{-\sinh u}{\cosh u + 2\cosh u_0} \tag{17}$$

and the initial relative extension is

$$\varepsilon_0 = \frac{-\sinh u_0}{3\cosh u_0} \tag{18}$$

We use the following form for the orientation parameter, $O = (3\langle\cos^2\theta\rangle - 1)/2$, where θ is the angle between the monomer direction and the positive direction of the x-axis, and $\langle\cos^2\theta\rangle$ is an average over all monomers. The orientation parameter equals 0 for arbitrarily oriented monomers, 1 for full longitudinal alignment, and −0.5 for full radial alignment. Using eq 16, the average segmental orientation of chains in the jet is given by

$$O = \frac{3}{2}(P_x^+ + P_x^-)\cos^2\theta - \frac{1}{2} = \frac{\cosh u - \cosh u_0}{\cosh u + 2\cosh u_0} \tag{19}$$

Note that $\cos^2\theta$ is not affected by the direction polarity and that the lateral components vanish because $\cos^2(\pi/2) = 0$. The probability that a monomer will be aligned with any of the three Cartesian axes, expressed in terms of O, can be obtained by inverting eq 19:

$$P_x = P_x^+ + P_x^- = \frac{1 + 2O}{3}$$

$$P_y = P_z = P_y^+ + P_y^- = \frac{1 - P_x}{2} = \frac{1 - O}{3} \tag{20}$$

The extension dependence of O can be extracted from eqs 17, 18, and 19:

$$O = \frac{-(1 - 3\varepsilon_0{}^2) + \sqrt{(1 - 9\varepsilon_0{}^2) + 3(1 + 3\varepsilon_0{}^2)\varepsilon^2}}{1 + 3\varepsilon_0{}^2} \tag{21}$$

which, for small values of ε_0, can be approximated within accuracy of $O(\varepsilon_0{}^2)$ by

$$O \cong -1 + \sqrt{1 + 3\varepsilon^2}, \quad \varepsilon_0 \ll 1 \tag{22}$$

The orientation of eq 21 is depicted in Figure 5, with ε expressed in terms of the relative strain rate s/s_c (eqs 11 and
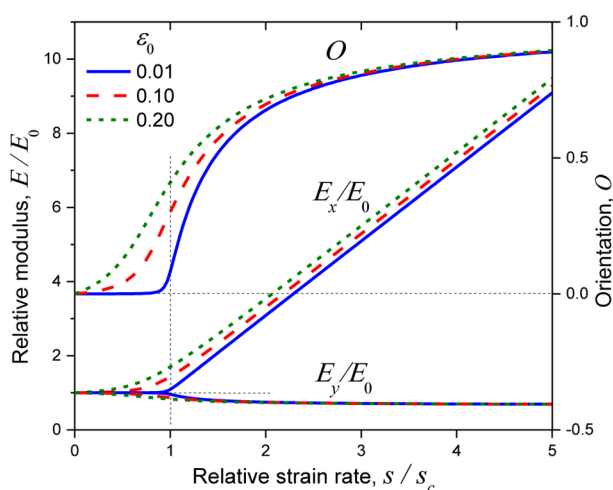
Figure 5. Orientation O and relative tensile modulus E/E_0 as functions of the relative strain rate s/s_c, where $s_c = 3\tau^{-1}$ is the critical strain rate (τ is the chain relaxation time), and E_0, E_x, and E_y are the isotropic, longitudinal, and transverse tensile moduli, respectively. The orientation and moduli are given by eqs 21 and 24, respectively. The tensile moduli of an aggregate's unit element are related by the ratio $E_1/E_2 \gg 1$, where E_1 and E_2 are the longitudinal and transverse moduli of the element.

14), exhibiting a similar abrupt rise as ε at the critical strain rate. Note that at zero strain rate, although each of the aggregate's unit elements has an initial extension ε_0, the resulting orientation tends to zero because the elements are randomly oriented ($u_x = u_y = u_z = u_0$).

■ NANOFIBER ELASTIC MODULUS

The extension of chains in the polymer solution reaches a steady state very fast and is therefore retained during solidification of the jet and formation of a nanofiber. Even though some chain relaxation, that is, recoiling, occurs after the stretching stress is relieved, it is limited due to solidification and interaction with neighboring chains (see Supporting Information section S6). Hence, the degree of chain elongation during the liquid phase of the jet, expressed by the relative extension ε or the segmental orientation O, can be used as an estimate for the conformation of the polymer chains in the solid phase, namely, the nanofiber. The average segmental orientation

affects the average elastic properties of the solid polymer because the elastic properties of such a segment are anisotropic. Here we use an aggregate representation[61,62] of the solid to estimate the polymer elastic properties, predominantly its stiffness in tension. Aggregate models were used successfully in predicting the properties of anisotropic amorphous polymers formed, for example, by cold or hot drawing, as well as in crystalline polymers.[61,62] More recently, Pai et al. used Ward's aggregate model to predict the elastic modulus of electrospun PA 6(3)T nanofibers using measured molecular orientation.[6]

Consider a typical rigid chain segment (Kuhn monomer), representing a single unit element in the polymer aggregate, shown in Figure 4 in a local Cartesian system 1, 2, 3. The elasticity of the segment is assumed to be transversely isotropic, with an axis of symmetry 1 and a plane of isotropy 2–3, such that the element's stiffness in the axial direction (1) is high, dominated by the covalent bonds along the chain backbone, whereas in the lateral (transverse) directions (2, 3) the stiffness is dominated by the much lower intermolecular forces such as van der Waals. Such a unit element has five independent elastic stiffness constants, defined in engineering notation as the elastic moduli E_1, E_2, G_{12}, ν_{12}, and ν_{23}. As suggested in the previous section, the chain segments are assumed to be aligned with the three axes x, y, z of a global Cartesian system (that is, a lattice), where x is the nanofiber main axis and y, z are the lateral (radial) axes. This assumption, namely, that the segments' alignment is confined to the directions of the system axes, is justified statistically in view of the very large number of segments in the aggregate.

Given an average segmental orientation O and the corresponding orientation probabilities from eq 20, the five engineering stiffness constants of the nanofiber, E_x, E_y, G_{xy}, ν_{xy}, and ν_{yz}, can be obtained from the unit element properties (see Supporting Information section S1). We focus here on the axial and lateral tensile moduli, E_x and E_y, respectively, for which a plain iso-stress mixing rule can be used:

$$\frac{1}{E_x} = \frac{P_x}{E_1} + \frac{P_y + P_z}{E_2} = \frac{1}{3}\left[\left(\frac{1}{E_1} + \frac{2}{E_2}\right) - \left(\frac{2}{E_2} - \frac{2}{E_1}\right)O\right]$$

$$\frac{1}{E_y} = \frac{P_y}{E_1} + \frac{P_x + P_z}{E_2} = \frac{1}{3}\left[\left(\frac{1}{E_1} + \frac{2}{E_2}\right) + \left(\frac{1}{E_2} - \frac{1}{E_1}\right)O\right] \tag{23}$$

By doing so, we sum up the compliances (that is, E^{-1}) of all the elements in a row in the x direction (Figure 4) and similarly all the elements in a row in the y direction. The assumed iso-stress condition was preferred over iso-strain (Supporting Information section S2) as it better predicts the high modulus rise observed in experiments. Hence, the axial and lateral tensile moduli, normalized by the isotropic modulus E_0, are given by

$$\frac{E_x}{E_0} = \frac{1}{1 - \alpha_E O}$$

$$\frac{E_y}{E_0} = \frac{1}{1 + \frac{1}{2}\alpha_E O} \tag{24}$$

where the isotropic modulus is obtained by substituting $O = 0$ in eq 23:

$$E_0 = \frac{3E_1 E_2}{2E_1 + E_2} \cong \frac{3}{2}E_2 \tag{25}$$

and α_E is an engineering constant slightly smaller than 1:

$$\alpha_E = \frac{2E_1/E_2 - 2}{2E_1/E_2 + 1} \cong 1 \tag{26}$$

The maximum theoretically achievable axial tensile modulus occurs when $O = 1$ and equals E_1, yielding

$$\left(\frac{E_x}{E_0}\right)_{max} = \frac{2E_1/E_2 + 1}{3} \cong \frac{2}{3}\frac{E_1}{E_2} \tag{27}$$

Similarly, the minimum theoretical lateral modulus equals E_2, yielding

$$\left(\frac{E_y}{E_0}\right)_{min} = \frac{2E_1/E_2 + 1}{3E_1/E_2} \cong \frac{2}{3} \tag{28}$$

The approximations in eqs 25−28 assume that $E_1 \gg E_2$, justified when considering the relative elastic stiffness of covalent bonds ($\sim E_1$) and intermolecular bonds ($\sim E_2$), which is in the order of $E_1/E_2 \sim 10^2 – 10^3$.[63,64] Also, typical measured ratios for partially oriented drawn and compacted polymers vary between 10 and 50.[62] Hence, the maximum saturation value is of order $E_x/E_0 \sim 10^2 – 10^3$, possibly achievable in pure crystalline structures,[65] whereas for amorphous and semicrystalline polymers it is likely in between the iso-stress result and the much lower iso-strain result (Supporting Information section S2).

Equation 24 provides a very simple yet meaningful prediction for the tensile moduli of a polymer whose structure can be represented by an aggregate. This minimalistic result, uncommon in models of structural anisotropy with molecular orientation,[6,62] is made possible owing to the use of the lattice representation of polymer chains. Similar trends of sharp rise in the longitudinal modulus and moderate drop in the transversal modulus were observed experimentally in cold drawn polymers in relation to the draw ratio, a parameter that corresponds to segmental orientation.[62] Furthermore, it is seen that the moduli depend predominantly on the molecular orientation set in the solid nanofiber, regardless of how it was reached and the polymer type, in agreement with experimental observations[62] made on cold drawn polymers. Although the aggregate modeling has some limitations, in that it generates widely separated upper and lower bounds for the moduli (because, due to anisotropy, when assuming uniform stress the strain in the aggregate is not uniform, and vice versa),[62] it still provides a good prediction for the longitudinal modulus, as shown in the next section.

The application of this result to electrospun nanofibers is done by substituting the strain rate dependence of the relative extension ε (eq 11) into the orientation in eq 21. The resulting strain rate dependence of the tensile moduli is depicted in Figure 5. The rise of the longitudinal modulus at high strain rates is linear with the strain rate, as can be shown by using eqs 13, 14, and 22. Approximating by series expansion at accuracy $O[(s/s_c)^{-2}]$, we obtain $O \cong 1 - (s/s_c)^{-1}/2$, which when substituted in eq 24 with $\alpha_E = 1$ ($E_1 \gg E_2$) yields

$$\frac{E_x}{E_0} \cong 2\frac{s}{s_c}, \quad s \gg s_c \tag{29}$$

This rise is limited by the maximum theoretically achievable modulus (eq 27) and by electrospinnability[23] bounds.

This modulus−strain rate dependency can be further expressed in terms of the electrospinning process parameters such as the electric field intensity, solution concentration, and solution feed rate. Using the known dependence of s on these parameters[23,45,46] and the critical s_c from eq 14, the relative strain rate scales as (details are provided in the Supporting Information section S5)

$$\frac{s}{s_c} = \frac{s\tau}{3} \propto \frac{b^3 D_0^{1/3}\eta_s^{1/6}\sigma_e^{1/2}E^{5/3}}{v_0^{1/3}N^{1/2}} \begin{cases} \phi^{-(2\nu+3)/[2(3\nu-1)]} & \text{good solvent} \\ \phi^{-26/9} & \theta\text{-solvent} \end{cases} \tag{30}$$

It is seen that the relative strain rate, and consequently the longitudinal modulus, increase upon an increase in the Kuhn segment length b, the injection diameter D_0, solvent viscosity η_s, solution electric conductivity σ_e, and electric field intensity E and upon a decrease in the jet initial velocity v_0 (alternatively, the feed rate), degree of polymerization N (alternatively, the molar mass), and polymer volume concentration in the solution ϕ. In general, the modulus will increase when a high stretching force is applied on a low-viscosity jet fed at low rate. The exponents of ϕ are close, −2.73 for a good solvent and −2.89 for a θ-solvent, meaning that the solvent dependence of the relative strain rate, and hence the relative longitudinal modulus, should be moderate. Equation 30 is powerful because it makes it possible to relate both the moduli and diameter (next section) directly to the electrospinning conditions as well as to determine the process conditions that can yield improvement of the mechanical properties (Supporting Information section S5).

■ CRITICAL DIAMETER AND MODULUS RISE

The condensed polymer network diameter scales as $D \approx D_{jet}\sqrt{\phi}$, where ϕ is the polymer volume fraction in the solution and D_{jet} is the local jet diameter.[6,23,66] For a given volume-conserving flow rate, the jet velocity and diameter are related by $v/v_0 \approx (D_{jet}/D_0)^{-2}$, where D_0 is the jet initial diameter (that is, the internal diameter of the injection needle, Figure 1b). Thus, the condensed polymer diameter D scales as[23]

$$\frac{D}{D_0} \approx \sqrt{\frac{\phi v_0}{v}} \tag{31}$$

The velocity profile at a constant strain rate is $v \cong sx$, and therefore the velocity upon reaching the collector is sd, where d is the gap distance between the electrodes (Figure 1a). Hence, the nanofiber diameter scales as

$$\frac{D}{D_0} \approx \sqrt{\frac{\phi v_0}{sd}} \tag{32}$$

Switching from the velocity domain v to the time domain t by substituting $v = v_0 e^{st}$, we can get the jet strain, $st \cong 2\ln(\sqrt{\phi}D_0/D(t))$, which is the Hencky strain (with the term $\sqrt{\phi}$ added for the condensed polymer) defined by McKinley and Sridhar[35] and used by Pai et al.[6] to determine the nanofiber drawing ratio.

We define the critical diameter D_c (or crossover diameter) as the nanofiber diameter obtained for a jet having a strain rate equal to the critical strain rate, $s = s_c = 3\tau^{-1}$ (eq 14):

$$\frac{D_c}{D_0} \approx \sqrt{\frac{\phi v_0}{s_c d}} \approx \sqrt{\frac{\phi v_0 \tau}{3d}} \approx N\phi^{\nu/(3\nu-1)}\sqrt{\frac{v_0\tau_0}{3d}} \tag{33}$$

The right term was obtained by substituting the expression for τ from eq 6. The exponent of ϕ is 0.77 for a good solvent and 1 for a θ-solvent. The critical diameter signifies the transition in

the molecular orientation and elastic moduli. The higher the D_c, the higher the nanofiber diameter where the tensile modulus starts to rise, and vice versa. The dependence of D_c on the degree of polymerization, solution concentration, solvent condition, initial velocity, electrodes gap, and solvent viscosity makes it controllable over a wide nanoscale and microscale range. In fact, except for the electric field intensity and the solution's electric conductance, all the free parameters of the electrospinning process are present in eq 33 (see eq 30). However, electrospinnability sets lower and upper bounds, for example, a high value of the quantity $N\phi^{\nu/(3\nu-1)}$ can result in excessively high solution viscosity that precludes jet formation, whereas a low value can result in complete disentanglement of the network and jet separation.[23] For that reason, the selection of N and ϕ values is typically balanced for a successful electrospinning process.

Combining eqs 32 and 33, we get

$$\frac{D}{D_c} \approx \left(\frac{s}{s_c}\right)^{-1/2} \tag{34}$$

where s/s_c can also be expressed in terms of the electrospinning process parameters (eq 30). We see that for $s < s_c$, a small increase in strain rate results in a sharp drop in diameter. This relationship enables us to depict the orientation and tensile moduli as functions of the relative diameter (Figure 6), by
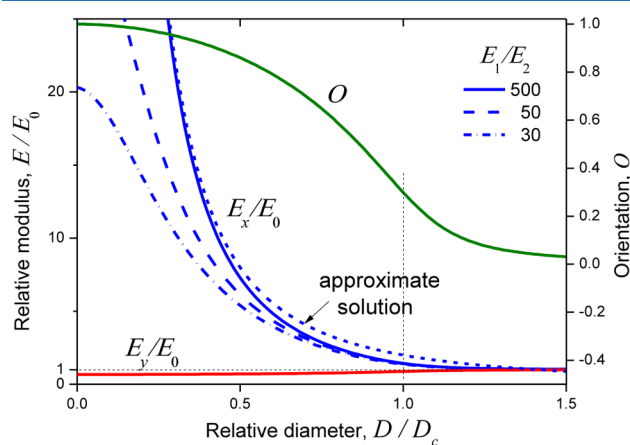
Figure 6. Orientation O and relative tensile modulus E/E_0 as functions of the relative fiber diameter D/D_c, where D_c is the critical diameter, and E_0, E_x, and E_y are the isotropic, longitudinal, and transverse tensile moduli, respectively. The orientation is given by eq 21. The tensile moduli are given by eq 24, and the longitudinal modulus approximation (short-dashed line) by eq 35. The initial extension is $\varepsilon_0 = 0.1$. The tensile moduli of an aggregate's unit element are related by the ratio E_1/E_2, where E_1 and E_2 are the longitudinal and transverse moduli of the element.

replacing the variable $s\tau$ in eq 11 by D/D_c (with the help of eq 14). The ratio E_1/E_2 sets the saturation value of the modulus $(D/D_c \to 0)$ at $E_x/E_0 \cong (2/3)E_1/E_2$ (eq 27). The lateral modulus decreases to the saturation value of $E_y/E_0 \cong 2/3$. The curves of O and E_x have opposite convexities at the region $D < D_c$, so that upon decreasing diameter, when O starts to rise sharply E_x rises moderately, then both rise sharply, and finally the trend reverses. This may possibly clarify why some experimental observations exhibit low correlation between modulus rise and orientation rise,[1] while other observations show higher correlation.[6,11,12]

Using eqs 13 and 22, and approximating by series expansion at accuracy $O[(D/D_c)^4]$, we obtain $O \cong 1 - (D/D_c)^2/2$, which when substituted in eq 24 yields a simple estimate for the longitudinal tensile modulus at diameters smaller than the critical diameter:

$$\frac{E_x}{E_0} \cong \left[(1 - \alpha_E) + \frac{\alpha_E}{2}\left(\frac{D}{D_c}\right)^2\right]^{-1} \cong 2\left(\frac{D}{D_c}\right)^{-2}, \quad D < D_c \tag{35}$$

where the right term is for $\alpha_E = 1$ ($E_1 \gg E_2$). This result is depicted in Figure 6 as the approximate solution. Similarly for diameters larger than the critical diameter, using eq 12 $O \cong 3\varepsilon_0^2(D/D_c)^{-2}$ at accuracy $O[(D/D_c)^{-4}]$, and the longitudinal tensile modulus approximation is

$$\frac{E_x}{E_0} \cong 1 + 3\varepsilon_0^2\left(\frac{D}{D_c}\right)^{-2}, \quad D > D_c \tag{36}$$

At the transition point, with the help of eqs 15 and 21, the critical longitudinal tensile modulus is approximated by

$$\left(\frac{E_x}{E_0}\right)_c \cong 1 + \frac{3\alpha_E}{2}\left(\frac{3\varepsilon_0}{2}\right)^{2/3} \cong 1 + 2\varepsilon_0^{2/3}, \quad D = D_c \tag{37}$$

where the right term is for $\alpha_E = 1$. Note that this value, typically below 2, only marks the beginning of the modulus climb, whereas the sharp rise is seen to occur at D/D_c below 0.5 and even lower (Figure 6).

Equation 35 demonstrates that when $D < D_c$, the dependence of the longitudinal modulus on the relative diameter is practically invariant with respect to the electrospinning conditions, such as the electric field, feed rate, solution concentration, and solvent condition (shown in eq 30). Moreover, by observing the accurate solution of the modulus in eq 24, we see that in addition to its dependence on α_E and D/D_c it depends only on ε_0 given by eq 9, which in turn depends on the solution concentration and solvent condition. However, this dependence is week, as seen in eq 37, Figure 5, and Figure 6. That said, the critical diameter does depend heavily on electrospinning conditions, as explained by eq 33, but this has no effect when D is normalized by D_c. More details on the effect of electrospinning conditions are provided in Supporting Information section S5.

Because the relative modulus is asymptotic to $E_x/E_0 = 1$ for large diameters, we can use eq 35 in the following form for the whole range of diameters:

$$\frac{E_x}{E_0} \cong 1 + 2\left(\frac{D}{D_c}\right)^{-2} \tag{38}$$

This approximation converges to the large and small diameters' asymptotes but does not provide an accurate description of the transition zone. It is interesting to note that this result bears some similarity in form (but differs in prefactor and exponent) with that obtained by the confinement approach[22] under completely different premises.

The resulting theoretical longitudinal modulus compares well with experimental data imported from studies published by Sui et al.,[4,8] Burman et al.,[1,3,7] Liu et al.,[5] Ji et al.,[2] Stachewicz et al.,[9] Papkov et al.,[10] and Pai et al. (data diluted to avoid masking of the other data sets),[6] which used a variety of polymers

(amorphous and semicrystalline), solutions, molar masses, and measurement techniques (Figure 7). Each data set is fitted to
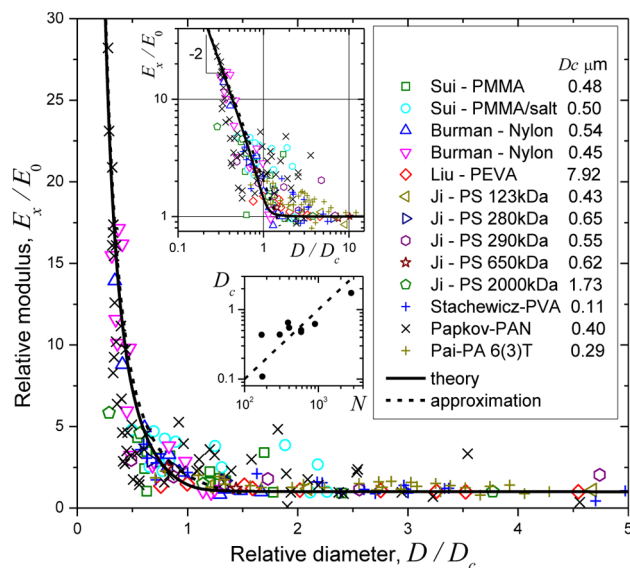
Figure 7. Experimental and theoretical relative longitudinal modulus E_x/E_0 as functions of the relative fiber diameter D/D_c, where D_c is the critical diameter and E_0 and E_x are the isotropic and longitudinal tensile moduli, respectively. The experimental data are imported from published studies[1–10] and are normalized by an estimated E_0. The critical diameter used to normalized each data set is noted in the legend. The theoretical solution (solid line) is given by eq 24 with $\alpha_E = 1$ and is for initial extension $\varepsilon_0 = 0.1$. The approximate solution for small diameters (dashed line) is given by eq 35, and its power slope (−2) is indicated on the log−log plot in the top inset. The R-squared value of the fit is $R^2 \cong 0.8$. Bottom inset: D_c vs the degree of polymerization N (where data was available), with a line $D_c \propto N$ (see eq 33).

the theoretical solution, and its D_c is extracted. The approximate power slope (−2) predicted in eq 35 is confirmed by the log−log plot in the top inset. The values of D_c span a wide range of 0.11−7.9 μm, with most common values in the range of 400−650 nm. The polymers degree of polymerization N varies between 108 and 2770 Kuhn segments, and D_c is seen to increase proportionally with N (bottom inset), as predicted by eq 33. Such dependency was also observed by Ji et al.,[2] although with $D_c \propto N^{0.6}$ rather than $D_c \propto N$. The data in Figure 7 are somewhat dispersed, as would be expected from the several parametric dependencies of D_c in eq 33, most notably the solution concentration and feed rate which could have been varied during some of the tests. Note that the maximum saturation value of E_x/E_0 is far below the limit found in eq 27 for iso-stress condition, setting a high bar for future improvement.

■ STRENGTH AND TOUGHNESS RISE

The study published by Sui et al.,[4,8] and the pursuing study by Papkov et al.,[10] contain additional data on the relationship between the diameter of electrospun nanofibers and their strength and toughness, not available in the other studies cited in Figure 7, allowing validation of further theoretical evaluation. In addition, yield strength versus diameter data are available from Pai et al.[6] At the scale of the aggregate's unit element (that is a Kuhn monomer), dominated by inchain and interchain interatomic bonds, we may assume a linear dependence

between strength and elastic modulus (the interatomic rupture strain is invariant).[63,64] Hence, we can write the strength of the polymer aggregate by replacing the elastic components in eqs 24−26 with the corresponding strengths components:

$$\frac{\sigma_x}{\sigma_0} = \frac{1}{1 - \alpha_\sigma O}$$

$$\frac{\sigma_y}{\sigma_0} = \frac{1}{1 + \frac{1}{2}\alpha_\sigma O} \tag{39}$$

By doing so, we sum up the "weaknesses" (that is, σ^{-1}) of all the elements in a row in the x direction (Figure 4), and similarly all the elements in a row in the y direction, in an analogous way to the summing up of compliances in eq 23. In this way, the weakest links in a given direction (that is, the links representing intermolecular bonds of strength σ_2) have a significant impact on the aggregate strength, as should be expected.

The isotropic strength is given at $O = 0$:

$$\sigma_0 = \frac{3\sigma_1\sigma_2}{2\sigma_1 + \sigma_2} \cong \frac{3}{2}\sigma_2 \tag{40}$$

and α_σ is an engineering constant slightly smaller than 1:

$$\alpha_\sigma = \frac{2\sigma_1/\sigma_2 - 2}{2\sigma_1/\sigma_2 + 1} \cong 1 \tag{41}$$

The maximum theoretically achievable strength occurs when $O = 1$ and equals σ_1, yielding

$$\left(\frac{\sigma_x}{\sigma_0}\right)_{max} = \frac{2\sigma_1/\sigma_2 + 1}{3} \cong \frac{2}{3}\frac{\sigma_1}{\sigma_2} \tag{42}$$

The approximations in eqs 40−42 are based on the notion that $\sigma_1 \gg \sigma_2$ because the strength of covalent bonds ($\sim\sigma_1$) is much higher than that of intermolecular bonds ($\sim\sigma_2$).[63,64] The estimate for the longitudinal tensile strength at diameters smaller than the critical diameter is (by analogy to eq 35), using the approximation $O \cong 1 - (D/D_c)^2/2$ as before

$$\frac{\sigma_x}{\sigma_0} \cong \left[(1 - \alpha_\sigma) + \frac{\alpha_\sigma}{2}\left(\frac{D}{D_c}\right)^2\right]^{-1} \cong 2\left(\frac{D}{D_c}\right)^{-2}, \quad D < D_c \tag{43}$$

The resulting theoretical longitudinal strength compares reasonably well with the strength experimental data imported from the studies published by Sui et al.,[4,8] Pai et al.,[6] and Papkov et al.[10] (Figure 8a).

For the purpose of assessing the effect of molecular orientation on the nanofiber toughness, we use the deformation work density W as a measure, where W_x is the energy per unit volume absorbed during a longitudinal tensile deformation, obtained by integrating the area underneath the stress−strain curve. The elastic portion of the work density scales as

$$\frac{W_x^{el}}{W_0^{el}} \approx \frac{(\sigma_x/\sigma_0)^2}{E_x/E_0} \approx \frac{1 - \alpha_E O}{(1 - \alpha_\sigma O)^2} \approx 2\left(\frac{D}{D_c}\right)^{-2} \tag{44}$$

where $W^{el} = \sigma^2/(2E)$ and the right term is for diameters smaller than the critical diameter, using the approximation $O \cong 1 - (D/D_c)^2/2$ with $\alpha_\sigma = \alpha_E = 1$. This work is equivalent to the elastic energy released when the nanofiber breaks.
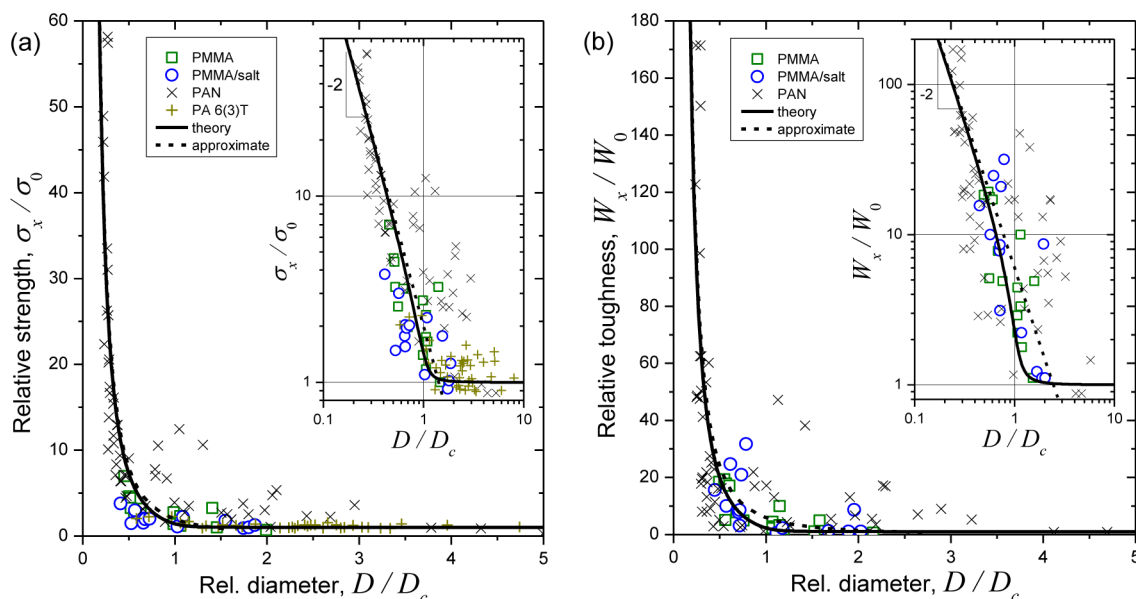
Figure 8. Experimental and theoretical relative strength and toughness as functions of the relative fiber diameter D/D_c, where D_c is the critical diameter. The experimental data are imported from the studies published by Sui et al.,[4,8] Pai et al. (yield strength, data diluted),[6] and Papkov et al.[10] The critical diameters used to normalize each data set are as in Figure 7, up to a constant prefactor close to unity. (a) Relative strength σ_x/σ_0, where σ_0 and σ_x are the isotropic and longitudinal tensile strengths, respectively. The theoretical solution (solid line) is given by eq 39 with $\alpha_\sigma = 1$ and is for initial extension $\varepsilon_0 = 0.1$. The theoretical approximation (dashed line) is given by eq 43, and its power slope (−2) is indicated on the log−log plot in the inset. The R-squared value of the fit is $R^2 \cong 0.8$. (b) Relative deformation work density W_x/W_0, where W_0 and W_x are the isotropic and longitudinal work densities, respectively. The theoretical solution (solid line) is given by eq 45 with $\alpha_\sigma = 1$ and is for initial extension $\varepsilon_0 = 0.1$. The theoretical approximation is given by eq 46, and its power slope (−2) is indicated on the log−log plot in the inset. The R-squared value of the fit is $R^2 \cong 0.6$.

When the segmental orientation along the deformation direction is high, interchain slippage increases and consequently the plastic elongation increases. In other words, chains mobility in the deformation direction increases. Increased chain mobility was evidenced in decreased glass transition temperature T_g while decreasing nanofibers diameter.[11,67] Given the probability P_x that a monomer will be aligned with the longitudinal axis (eq 20), we can say that the plastic strain (that is, elongation) in that direction scales as P_x. In other words, the elongation is assumed to be proportional to the fraction of aligned segments in the aggregate, P_x. This assumption is supported by the elongation experimental data from Sui et al.,[4,8] presented in Supporting Information section S3. Hence, the plastic portion of the work density may be scaled by $W_x^{pl} \approx P_x\sigma_x$, assuming the stress throughout the plastic deformation is approximately constant and its average is equal to the strength σ_x. This scaling bears similarity to the energy absorbed during plastic pullout of an aligned reinforcing filler from a matrix, $G \approx V_f\sigma_m l$,[68] where V_f is the filler volume fraction (analogous to P_x), σ_m is the matrix strength (analogous to σ_x), and l is the filler length scale (analogous to b, the monomer length). Using eq 39 for σ_x

$$\frac{W_x^{pl}}{W_0^{pl}} \approx \frac{P_x\sigma_x}{P_0\sigma_0} \approx \frac{1 + 2O}{1 - \alpha_\sigma O} \approx 6\left(\frac{D}{D_c}\right)^{-2} \tag{45}$$

where the right term is for diameters smaller than the critical diameter, using the approximation for O as before with $\alpha_\sigma = 1$ and $O \to 1$. The scaling of the total work (elastic and plastic) absorbed during fracture can be estimated by

$$\frac{W_x}{W_0} \approx \frac{W_x^{el} + W_x^{pl}}{W_0^{el} + W_0^{pl}} \approx 6\left(\frac{D}{D_c}\right)^{-2} \tag{46}$$

where the right term is for diameters smaller than the critical diameter, using the same assumptions as before and the notion that $E \gg \sigma$. We see that the contribution of the elastic deformation energy is negligible. The prefactor in this estimate may vary with respect to the assumptions used in this analysis; however, the scaling dependence of the fracture energy on D^{-2} seems solid.

The total work approximation is depicted in Figure 8b and is compared with the toughness experimental data imported from the studies published by Sui et al.[4,8] and Papkov et al.[10] The scaling and prefactor in eq 46 are generally corroborated by this experimental evidence, even though the data are noticeably dispersed, keeping in mind that the toughness is affected by several parameters including modulus, strength, and chain mobility. These results show a significant increase in toughness, which scales with $(D/D_c)^{-2}$, as found for the stiffness and strength but with a different prefactor. The improvement in toughness is much more significant than the parallel improvement in stiffness and strength (3 times higher); that is, toughness responds more vigorously to the degree of orientation. Furthermore, the increase in the plastic deformation energy is 3 times higher than in the elastic energy.

The improvement in toughness at small nanofiber diameters is achieved most probably by favoring intermolecular sliding over tearing of covalent bonds. It was also suggested that toughness increases as a result of increased chain mobility due to low degree of crystallinity (found in small diameter electrospun PAN nanofibers),[10] yet the sharp rise in toughness occurs in noncrystalline polymers as well (PMMA nanofibers)[4,8] (see Figure 8b). Another possible influencing factor is structural defects due to interchain free volume and to porosity caused by rapid solvent evaporation. Such defects, which could vary as a result of stretching, molecular orientation, and

diameter shrinking, seem to account for the wide scattering of the elongation experimental data[4,8,10] (Supporting Information section S3).

The reason for the great improvement in toughness is that toughness gains from two simultaneous mechanisms, both associated with enhanced molecular orientation: the strengthening mechanism due to anisotropy and the interchain sliding mechanism due to alignment. At a high degree of orientation (that is, at small diameters), the strengthening mechanism exhibits a sharp rise (the denominator in eq 45 tends to zero), whereas the sliding mechanism exhibits a moderate rise and saturates (the numerator in eq 45 tends to a constant value; see Supporting Information section S3). At high orientation, because the longitudinal strength is strongly affected by the weak links in the aggregate (the laterally aligned monomers), a small decrease in the fraction of such links has a sharp positive effect on the strength, whereas the elongation has already reached saturation and is only marginally affected.

■ CONCLUSION

The simultaneous stretching and partial retraction of polymer chains, under a constant strain rate extensional flow of a polymer solution, reaches a steady chain extension early on. Accordingly, the average segmental orientation, derived from the extended conformation of the polymer chains, reaches a steady value. The model shows that both extension and orientation are going through an abrupt transition at a critical strain rate, reminiscent of the known phenomenon of coil stretch transition of a free unentangled chain, but occurring here for a chain entangled in a network. Below the critical strain rate chains are only slightly stretched but remain essentially coiled, whereas above it they are highly stretched. The critical strain rate is inversely proportional to the relaxation time of an extended chain.

In the case of an electrospinning jet, the extended chain nonequilibrium conformation is essentially retained in the solid nanofiber as a result of the very fast solvent evaporation. The nanofiber is represented by an aggregate of transversely isotropic unit elements having directions corresponding to the orientation probabilities. Each element is a chain segment with high longitudinal stiffness and low lateral stiffness, reflecting the intra- and intermolecular interactions of the segment, respectively. For a given segmental orientation, the aggregate's elastic moduli (stiffness constants) are calculated, exhibiting an abrupt transition in relation to the flow's critical strain rate, followed by a linear dependence on the strain rate.

The nanofiber diameter depends on the flow strain rate as well, making it possible to relate between the elastic moduli and the diameter. This relationship should not be construed as an evidence for size dependence of the moduli, as these quantities (that is, diameter and modulus) are only interrelated by association through the strain rate. That said, the model shows an abrupt rise in the longitudinal modulus for diameters smaller than the critical diameter and at the same time a moderate decrease in the lateral modulus. The critical diameter is not universal but rather depends widely on process parameters. A scaling law is derived, where the modulus sharp rise is inversely proportional to the nanofiber diameter squared, conforming to wide experimental evidence.

Similar dependencies, backed by experimental evidence, are derived for the nanofiber strength and toughness, exhibiting a simultaneous rise with the elastic stiffness. The rise in toughness was found to be more significant than in stiffness

and strength, as it gains from both the increased strength and increased chains mobility. The dependence of the stiffness, strength and toughness on process rather than size presents a simple path for tuning the mechanical properties of as-spun nanofibers. Finally, the theoretical saturation values are much higher than the maximum values observed in experiments, setting a high goal for future improvement in the mechanical properties of nanofibers. In view of the high interest in the reinforcement of electrospun nanofibers with nanofillers such as carbon nanotubes (CNTs),[11] an analysis of such a nanocomposite structure, based on the approach of the current paper, is included in Supporting Information section S4.

■ APPENDIX. CALCULATION OF HYDRODYNAMIC FRICTION AND INITIAL EXTENSION

The polymer network structure determines the chain elasticity and hydrodynamic friction. A polymer chain in a semidilute solution consists of correlation blobs (equivalent to network cells), which are smaller than the entanglement strands. Because the blobs are space-filling (there are no gaps between network cells), excluded volume interactions are screened by neighboring chains, and the chain can be regarded as an ideal chain of blobs (that is, a random walk of blobs).[32] The chain has N/g such blobs, each contains $g \approx \phi^{-1/(3\nu-1)}$ monomers and has a size $\xi \approx b\phi^{-\nu/(3\nu-1)}$ for a θ-solvent and an athermal solvent (the high temperature limit of a good solvent), where ν is Flory's exponent (1/2 for a θ-solvent and approximately 0.588 for a good solvent).[32] Because the space is completely filled with correlation blobs, hydrodynamic interactions are screened, and the Rouse model can be used in calculating the friction.[32] The hydrodynamic friction coefficient of a single correlation blob scales as $\eta_s\xi$, and therefore the coefficient for the complete chain scales as

$$\zeta \approx \frac{\eta_s \xi N}{g} \approx \eta_s b N \phi^{(1-\nu)/(3\nu-1)} \tag{47}$$

The exponent of ϕ is 0.54 for a good solvent and 1 for a θ-solvent. The θ-solvent condition marks the crossover between good and poor solvents. The friction coefficient may somewhat change along the jet flow as a result of very high extension ratios and substantial mass loss due to evaporation, but these effects are not expected to modify the overall scaling approach applied in the current analysis (see Supporting Information section S6).

The primitive path initial extension, $\varepsilon = \varepsilon_0$, is given by

$$\varepsilon_0 \approx \frac{L_0}{L_{max}} \approx \frac{l_0}{l_{max}} \approx N_{e1}^{-1/2} \begin{cases} \phi^{(1-\nu)/(3\nu-1)} & \text{good solvent} \\ \phi^{2/3} & \theta\text{-solvent} \end{cases} \tag{48}$$

where $l_0 \approx bN_{e1}^{1/2}\phi^{-\nu/(3\nu-1)}$ is an entanglement strand end-to-end length (Figure 1b) for an athermal solvent and $l_0 \approx bN_{e1}^{1/2}\phi^{-2/3}$ for a θ-solvent; $l_{max} \approx bN_{e1}\phi^{-1/(3\nu-1)}$ is a strand's fully extended length for an athermal solvent and $l_{max} \approx bN_{e1}\phi^{-4/3}$ for a θ-solvent; and N_{e1} is the number of monomers in a strand in a melt (a fixed value for a given polymer, of order 10^0–10^1).[32] For typical values of solution volume concentrations used in electrospinning, $\phi = 0.01$–0.4, we get a range for the typical initial extensions, $\varepsilon_0 \cong 0.01$–0.3. Electrospinning is also performed with polymer melts ($\phi = 1$), but the current study does not address this class.

ASSOCIATED CONTENT

S Supporting Information

The Supporting Information is available free of charge on the ACS Publications website at DOI: 10.1021/acs.macromol.6b01204.

Section S1: nanofiber engineering stiffness constants; section S2: iso-strain tensile moduli; section S3: diameter dependence of elongation; section S4: effect of reinforcing filler; section S5: dependence on electrospinning process parameters; section S6: effects of solvent evaporation and network deformation (PDF)

AUTHOR INFORMATION

Corresponding Author

*(I.G.) E-mail: green_is@netvision.net.il.

Notes

The authors declare no competing financial interest.

ACKNOWLEDGMENTS

REFERENCES

(1) Arinstein, A.; Burman, M.; Gendelman, O.; Zussman, E. Effect of supramolecular structure on polymer nanofibre elasticity. *Nat. Nanotechnol.* **2007**, *2* (1), 59−62.

(2) Ji, Y.; Li, C.; Wang, G.; Koo, J.; Ge, S.; Li, B.; Jiang, J.; Herzberg, B.; Klein, T.; Chen, S.; Sokolov, J. C.; Rafailovich, M. H. Confinement-induced super strong PS/MWNT composite nanofibers. *EPL* **2008**, *84* (5), 56002.

(3) Burman, M.; Arinstein, A.; Zussman, E. Free flight of an oscillated string pendulum as a tool for the mechanical characterization of an individual polymer nanofiber. *Appl. Phys. Lett.* **2008**, *93* (19), 193118.

(4) Sui, X. M.; Wagner, H. D. Tough Nanocomposites: The Role of Carbon Nanotube Type. *Nano Lett.* **2009**, *9* (4), 1423−1426.

(5) Liu, Y.; Chen, S.; Zussman, E.; Korach, C. S.; Zhao, W.; Rafailovich, M. Diameter-Dependent Modulus and Melting Behavior in Electrospun Semicrystalline Polymer Fibers. *Macromolecules* **2011**, *44* (11), 4439−4444.

(6) Pai, C. L.; Boyce, M. C.; Rutledge, G. C. Mechanical properties of individual electrospun PA 6(3)T fibers and their variation with fiber diameter. *Polymer* **2011**, *52* (10), 2295−2301.

(7) Burman, M.; Arinstein, A.; Zussman, E. Do surface effects explain the unique elasticity of polymer nanofibers? *Europhys. Lett.* **2011**, *96*, 16006.

(8) Sui, X. M.; Wiesel, E.; Wagner, H. D. Enhanced Mechanical Properties of Electrospun Nano-Fibers Through NaCl Mediation. *J. Nanosci. Nanotechnol.* **2011**, *11* (9), 7931−7936.

(9) Stachewicz, U.; Bailey, R. J.; Wang, W.; Barber, A. H. Size dependent mechanical properties of electrospun polymer fibers from a composite structure. *Polymer* **2012**, *53* (22), 5132−5137.

(10) Papkov, D.; Zou, Y.; Andalib, M. N.; Goponenko, A.; Cheng, S. Z. D.; Dzenis, Y. A. Simultaneously Strong and Tough Ultrafine Continuous Nanofibers. *ACS Nano* **2013**, *7* (4), 3324−3331.

(11) Richard-Lacroix, M.; Pellerin, C. Molecular Orientation in Electrospun Fibers: From Mats to Single Fibers. *Macromolecules* **2013**, *46* (24), 9473−9493.

(12) Richard-Lacroix, M.; Pellerin, C. Orientation and Partial Disentanglement in Individual Electrospun Fibers: Diameter Dependence and Correlation with Mechanical Properties. *Macromolecules* **2015**, *48* (13), 4511−4519.

(13) Cuenot, S.; Demoustier-Champagne, S.; Nysten, B. Elastic modulus of polypyrrole nanotubes. *Phys. Rev. Lett.* **2000**, *85* (8), 1690−1693.

(14) Cuenot, S.; Fretigny, C.; Demoustier-Champagne, S.; Nysten, B. Surface tension effect on the mechanical properties of nanomaterials measured by atomic force microscopy. *Phys. Rev. B: Condens. Matter Mater. Phys.* **2004**, *69* (16), 165410.

(15) Park, H. S.; Cai, W.; Espinosa, H. D.; Huang, H. C. Mechanics of crystalline nanowires. *MRS Bull.* **2009**, *34* (3), 178−183.

(16) Sharma, P.; Ganti, S.; Bhate, N. Effect of surfaces on the size-dependent elastic state of nano-inhomogeneities. *Appl. Phys. Lett.* **2003**, *82* (4), 535−537.

(17) Dingreville, R.; Qu, J. M.; Cherkaoui, M. Surface free energy and its effect on the elastic behavior of nano-sized particles, wires and films. *J. Mech. Phys. Solids* **2005**, *53* (8), 1827−1854.

(18) Camposeo, A.; Greenfeld, I.; Tantussi, F.; Pagliara, S.; Moffa, M.; Fuso, F.; Allegrini, M.; Zussman, E.; Pisignano, D. Local Mechanical Properties of Electrospun Fibers Correlate to Their Internal Nanostructure. *Nano Lett.* **2013**, *13* (11), 5056−5062.

(19) Camposeo, A.; Greenfeld, I.; Tantussi, F.; Moffa, M.; Fuso, F.; Allegrini, M.; Zussman, E.; Pisignano, D. Conformational evolution of elongated polymer solutions tailors the polarization of light-emission from organic nanofibers. *Macromolecules* **2014**, *47* (14), 4704−4710.

(20) Greenfeld, I.; Zussman, E. Controlling the Nanostructure of Electrospun Polmeric Fibers. In *Electrospinning for High Performance Sensors*; Macagnano, A., Zampetti, E., Kny, E., Eds.; Springer International Publishing: 2015; pp 35−64.

(21) Arinstein, A.; Zussman, E. Electrospun Polymer Nanofibers: Mechanical and Thermodynamic Perspectives. *J. Polym. Sci., Part B: Polym. Phys.* **2011**, *49* (10), 691−707.

(22) Arinstein, A. Confinement mechanism of electrospun polymer nanofiber reinforcement. *J. Polym. Sci., Part B: Polym. Phys.* **2013**, *51* (9), 756−763.

(23) Greenfeld, I.; Zussman, E. Polymer entanglement loss in extensional flow: evidence from electrospun short nanofibers. *J. Polym. Sci., Part B: Polym. Phys.* **2013**, *51* (18), 1377−1391.

(24) Greenfeld, I.; Arinstein, A.; Fezzaa, K.; Rafailovich, M. H.; Zussman, E. Polymer dynamics in semidilute solution during electrospinning: A simple model and experimental observations. *Phys. Rev. E* **2011**, *84* (4), 041806.

(25) Mead, D. W.; Larson, R. G.; Doi, M. A molecular theory for fast flows of entangled polymers. *Macromolecules* **1998**, *31* (22), 7895−7914.

(26) Archer, L. A. Polymer disentanglement in steady-shear flow. *J. Rheol.* **1999**, *43* (6), 1617−1633.

(27) Mhetar, V. R.; Archer, L. A. A new proposal for polymer dynamics in steady shearing flows. *J. Polym. Sci., Part B: Polym. Phys.* **2000**, *38* (1), 222−233.

(28) Shenoy, S. L.; Bates, W. D.; Frisch, H. L.; Wnek, G. E. Role of chain entanglements on fiber formation during electrospinning of polymer solutions: good solvent, non-specific polymer-polymer interaction limit. *Polymer* **2005**, *46* (10), 3372−3384.

(29) Wen, Y. H.; Hua, C. C. Chain stretch and relaxation in transient entangled solutions probed by double-step strain flows. *J. Rheol.* **2009**, *53* (4), 781−798.

(30) de Gennes, P. G. *Scaling Concepts in Polymer Physics*; Cornell University Press: Ithaca, NY, 1979; p 324.

(31) Doi, M.; Edwards, S. F. *The Theory of Polymer Dynamics*; Oxford University Press: New York, 1986.

(32) Rubinstein, M.; Colby, R. H. *Polymer Physics*; Oxford University Press: New York, 2003; p xi, 440 pp.

(33) Watanabe, H. Viscoelasticity and dynamics of entangled polymers. *Prog. Polym. Sci.* **1999**, *24* (9), 1253−1403.

(34) Ianniruberto, G.; Marrucci, G. A simple constitutive equation for entangled polymers with chain stretch. *J. Rheol.* **2001**, *45* (6), 1305−1318.

(35) McKinley, G. H.; Sridhar, T. Filament-stretching rheometry of complex fluids. *Annu. Rev. Fluid Mech.* **2002**, *34*, 375−415.

(36) Bhattacharjee, P. K.; Nguyen, D. A.; McKinley, G. H.; Sridhar, T. Extensional stress growth and stress relaxation in entangled polymer solutions. *J. Rheol.* **2003**, *47* (1), 269−290.

(37) Graham, R. S.; Likhtman, A. E.; McLeish, T. C. B. Microscopic theory of linear, entangled polymer chains under rapid deformation including chain stretch and convective constraint release. *J. Rheol.* **2003**, *47* (5), 1171−1200.

(38) Nguyen, T. Q.; Kausch, H. H. Chain Scission in Transient Extensional Flow Kinetics and Molecular-Weight Dependence. *J. Non-Newtonian Fluid Mech.* **1988**, *30* (2−3), 125−140.

(39) Odell, J. A.; Keller, A.; Muller, A. J. Thermomechanical Degradation of Macromolecules. *Colloid Polym. Sci.* **1992**, *270* (4), 307−324.

(40) Buchholz, B. A.; Zahn, J. M.; Kenward, M.; Slater, G. W.; Barron, A. E. Flow-induced chain scission as a physical route to narrowly distributed, high molar mass polymers. *Polymer* **2004**, *45* (4), 1223−1234.

(41) Kirichenko, V. N.; Petrianovsokolov, I. V.; Suprun, N. N.; Shutov, A. A. Asymptotic Radius of Slightly Conducting Liquid Jet in an Electric-Field. *Dokl. Akad. Nauk SSSR* **1986**, *289* (4), 817−820.

(42) Spivak, A. F.; Dzenis, Y. A. Asymptotic decay of radius of a weakly conductive viscous jet in an external electric field. *Appl. Phys. Lett.* **1998**, *73* (21), 3067−3069.

(43) Hohman, M. M.; Shin, M.; Rutledge, G.; Brenner, M. P. Electrospinning and electrically forced jets. II. Applications. *Phys. Fluids* **2001**, *13* (8), 2221−2236.

(44) Higuera, F. J. Stationary viscosity-dominated electrified capillary jets. *J. Fluid Mech.* **2006**, *558*, 143−152.

(45) Reznik, S. N.; Zussman, E. Capillary-dominated electrified jets of a viscous leaky dielectric liquid. *Phys. Rev. E* **2010**, *81* (2), 026313.

(46) Greenfeld, I.; Fezzaa, K.; Rafailovich, M. H.; Zussman, E. Fast X-ray Phase-Contrast Imaging of Electrospinning Polymer Jets: Measurements of Radius, Velocity, and Concentration. *Macromolecules* **2012**, *45* (8), 3616−3626.

(47) Casper, C. L.; Stephens, J. S.; Tassi, N. G.; Chase, D. B.; Rabolt, J. F. Controlling surface morphology of electrospun polystyrene fibers: Effect of humidity and molecular weight in the electrospinning process. *Macromolecules* **2004**, *37* (2), 573−578.

(48) Guenthner, A. J.; Khombhongse, S.; Liu, W. X.; Dayal, P.; Reneker, D. H.; Kyu, T. Dynamics of hollow nanofiber formation during solidification subjected to solvent evaporation. *Macromol. Theory Simul.* **2006**, *15* (1), 87−93.

(49) Arinstein, A.; Zussman, E. Postprocesses in tubular electrospun nanofibers. *Phys. Rev. E* **2007**, *76* (5), 056303.

(50) Dayal, P.; Liu, J.; Kumar, S.; Kyu, T. Experimental and theoretical investigations of porous structure formation in electrospun fibers. *Macromolecules* **2007**, *40* (21), 7689−7694.

(51) Dayal, P.; Kyu, T. Dynamics and morphology development in electrospun fibers driven by concentration sweeps. *Phys. Fluids* **2007**, *19* (10), 107106.

(52) Bellan, L. M.; Craighead, H. G.; Hinestroza, J. P. Direct measurement of fluid velocity in an electrospinning jet using particle image velocimetry. *J. Appl. Phys.* **2007**, *102* (9), 094308.

(53) Han, T.; Yarin, A. L.; Reneker, D. H. Viscoelastic electrospun jets: Initial stresses and elongational rheometry. *Polymer* **2008**, *49* (6), 1651−1658.

(54) Reneker, D. H.; Yarin, A. L.; Fong, H.; Koombhongse, S. Bending instability of electrically charged liquid jets of polymer solutions in electrospinning. *J. Appl. Phys.* **2000**, *87* (9), 4531−4547.

(55) Reneker, D. H.; Yarin, A. L.; Zussman, E.; Xu, H. Electrospinning of nanofibers from polymer solutions and melts. *Adv. Appl. Mech.* **2007**, *41*, 43−195.

(56) Cohen, A. A Pade Approximant to the Inverse Langevin Function. *Rheol. Acta* **1991**, *30* (3), 270−273.

(57) de Gennes, P. G. Coil-Stretch Transition of Dilute Flexible Polymers under Ultrahigh Velocity-Gradients. *J. Chem. Phys.* **1974**, *60* (12), 5030−5042.

(58) Odell, J. A.; Keller, A.; Miles, M. J. Assessment of Molecular Connectedness in Semi-Dilute Polymer-Solutions by Elongational Flow. *Polymer* **1985**, *26* (8), 1219−1226.

(59) Greenfeld, I.; Zussman, E. Polymer Network Dynamics during Electrospinning: Random Walk Simulation. In *Electrospinning: Principles, Practice and Possibilities*; Mitchell, G. R., Ed.; The Royal Society of Chemistry: 2015; pp 71−99.

(60) Feynman, R. P. *Statistical Mechanics; A Set of Lectures*; W. A. Benjamin: Reading, MA, 1972; p xii, 354 pp.

(61) Arridge, R. G. C. *Mechanics of Polymers*; Clarendon Press: Oxford, 1975; p ix, 246 pp.

(62) Ward, I. M.; Sweeney, J. *An Introduction to the Mechanical Properties of Solid Polymers*, 2nd ed.; Wiley: Chichester, 2004; p x, 382 pp.

(63) Ashby, F.; Jones, D. R. H. *Engineering Materials 1: An Introduction to Properties, Applications and Design*; Butterworth-Heinemann: 2011; p 496.

(64) Ashby, M. F.; Shercliff, H.; Cebon, D. *Materials: Engineering, Science, Processing and Design*, 3rd ed.; Butterworth-Heinemann: 2013.

(65) Treloar, L. R. G. Calculations of elastic moduli of polymer crystals: I. Polyethylene and Nylon 66. *Polymer* **1960**, *1* (1), 95−103.

(66) Fridrikh, S. V.; Yu, J. H.; Brenner, M. P.; Rutledge, G. C. Controlling the fiber diameter during electrospinning. *Phys. Rev. Lett.* **2003**, *90* (14), 144502.

(67) Curgul, S.; Van Vliet, K. J.; Rutledge, G. C. Molecular dynamics simulation of size-dependent structural and thermal properties of polymer nanofibers. *Macromolecules* **2007**, *40* (23), 8483−8489.

(68) Greenfeld, I.; Wagner, H. D. Nanocomposite toughness, strength and stiffness - the role of filler geometry. *Nanocomposites* **2015**, *1*, 3−17.